

# Three-dimensional optical tomographic brain imaging in small animals, part 1: hypercapnia

## A. Y. Bluestone

Columbia University  
Departments of Biomedical Engineering and Radiology  
New York, New York 10027  
and  
State University of New York  
Downstate Medical Center  
Department of Pathology  
Brooklyn, New York 11203

## M. Stewart

State University of New York  
Downstate Medical Center  
Department of Physiology and Pharmacology  
Brooklyn, New York 11203

## J. Lasker

## G. S. Abdoulaev

## A. H. Hielscher

Columbia University  
Departments of Biomedical Engineering and Radiology  
ET 351 Mudd Building, MC8904  
500 West 120 Street  
New York, New York 10027  
E-mail: ahh2004@columbia.edu

**Abstract.** In this study, we explore the potential of diffuse optical tomography for brain oximetry. While several groups have already reported on the sensitivity of optical measurements to changes in oxyhemoglobin, deoxyhemoglobin, and blood volume, these studies were often limited to single source-detector geometries or topographic maps, where signals obtained from within the brain are projected onto 2-D surface maps. In this two-part study, we report on our efforts toward developing a volumetric optical imaging system that allows one to spatially resolve 3-D hemodynamic effects in rat brains. In part 1, we describe the instrumentation, optical probe design, and the model-based iterative image reconstruction algorithm employed in this work. Consideration of how *a priori* anatomical knowledge can be incorporated in the reconstruction process is presented. This system is then used to monitor global hemodynamic changes that occur in the brain under various degrees of hypercapnia. The physiologic cerebral response to hypercapnia is well known and therefore allows an initial performance assessment of the imaging system. As expected, we observe global changes in blood volume and oxygenation, which vary linearly as a function of the concentration of the inspired carbon dioxide. Furthermore, experiments are designed to determine the sensitivity of the reconstructions of only 1 mm to inaccurate probe positioning. We determine that shifts can significantly influence the reconstructions. In part 2 we focus on more local hemodynamic changes that occur during unilateral carotid occlusion performed at lower-than-normal systemic blood pressure. In this case, the occlusion leads to a predominantly monohemispherically localized effect, which is well described in the literature. Having explored the system with a well-characterized physiologic effect, we investigate and discuss the complex compensatory cerebrovascular hemodynamics that occur at normotensive blood pressure. Overall, these studies demonstrate the potential and limitations of our diffuse optical imager for visualizing global and focal hemodynamic phenomenon three dimensionally in the brains of small animals. © 2004 Society of Photo-Optical Instrumentation Engineers. [DOI: 10.1117/1.1784471]

**Keywords:** optical tomography; brain imaging; hypercapnia; small animal imaging; rodents.

Paper 03077 received Jun. 17, 2003; revised manuscript received Jan. 14, 2004; accepted for publication Jan. 26, 2004.

## 1 Introduction

During the last 10 years there has been an increasing interest in small animal imaging systems.<sup>1–3</sup> This interest is motivated by progress in the transgenic manipulation of small animals that are used as models of human diseases and pathological conditions. By studying these animals, it is possible to link specific genes to normal and abnormal molecular, cellular, and organ functions. Studies of the biochemistry and physiology of the brain, heart, musculoskeletal, and metabolic systems have historically been through necropsy methods, which require the sacrificing of animals at different stages of disease

progression. Using these methods, it is not possible to study the temporal development of disease within a single animal. With the advent of novel small animal imaging systems, it is now feasible to perform noninvasive assays for the monitoring of both the temporal and spatial progression of disease and other biological processes in small living animals.

Besides positron emission tomography (PET), single photon emission tomography (SPECT), ultrasound (US), x-ray computed tomography (micro CT), and magnetic resonance imaging (MRI), diffuse optical tomography (DOT) has emerged as a potential small animal imaging modality. Commercial small animal optical imaging devices already exist for 2-D surface imaging of fluorescent or bioluminescent

Address all correspondence to: Andreas H. Hielscher, Columbia Univ., Dept. of Biomedical Engineering, ET351 Mudd Bldg, MC8904, 500 West 120th St, New York, NY 10027, USA. Tel: 212 854 5080; Fax: 212 854 8725; E-mail: ahh2004@columbia.edu

probes,<sup>4-8</sup> and recently Ntziachristos and Weissleder<sup>9</sup> have developed the first prototype for 3-D fluorescence imaging. Oximetry systems that provide spatially resolved images of various blood parameters in humans are commercially available through, for example, Hamamatsu, Hitachi, Somanetics, ISS, NIRx, and Techen. These and other systems have mainly been applied to human brain imaging,<sup>10-14</sup> where applications range from functional imaging to the examination of cerebral hemodynamics during ischemia.

In addition, several studies of small animal imaging using optical methods have already been performed in the area of small animal oximetry. Most of these works also focus on measurements in the brain. For example, Wolf et al.<sup>15</sup> reported as early as 1996 on the use of near-infrared (NIR) spectroscopy for noninvasive on-line detection of cortical spreading depression in a pentobarbital anesthetized rat. Transmitted NIR intensities were measured at four wavelengths with an optical probe consisting of one delivery fiber and one detection fiber placed over the intact skull about 6 mm apart. One year later, the same research group reported optical measurements of peri-infarct depolarization (PID) in focal cerebral ischemia in rats.<sup>16</sup> In this study, they performed a middle-cerebral artery occlusion to induce a focal ischemia. Near-infrared spectroscopy (NIRS) data were obtained every 2.5 s in arbitrary units as deflections from the baseline before the arterial occlusion. The authors concluded that NIRS is capable of noninvasive detection of a "fingerprint" of PID in rats. In 1999, Nemoto et al. carried out somatosensory stimulation studies in rats by stimulating the hind limb.<sup>17</sup> However, instead of imaging through the skin and skull, the bone was made translucent using a carboxymethyl polymer and only 2-D tomographic maps were generated by taking images with a charge-coupled device (CCD) camera. Siegel, Marota, and Boas,<sup>18</sup> in a paper on a new optical instrument design, showed as an example of the performance of the instrument, that they were capable of generating topographic maps of localized changes in cortical hemodynamics in response to somatosensory provocation in an anesthetized rat. For the image reconstruction they used an algorithm based on diffusion theory. Using a back-projection approach, Cheung et al.<sup>19</sup> generated topographical maps during hypercapnia provocations in rats. The maps were obtained with a frequency domain code for semi-infinite media. Most recently, Chen et al.<sup>20,21</sup> performed optical studies using an intracranial infarction model in rats. The NIR system used in this study operated in the continuous-wave mode and employed one source and one detector separated by 5 mm. This probe was placed sequentially on 20 different positions on the head of the rat, which resulted in a topographic map of optical density changes between pre- and post-middle cerebral artery occlusion. In addition, MRI images and staining techniques were used to identify the location of ischemia as well as estimate the area of the lesion. The authors report significant correlation among findings by near-infrared spectroscopy, MRI, and staining.

In all these cases, optical methods have been used to locate and quantify the concentration change of deoxyhemoglobin, oxyhemoglobin, and total hemoglobin during certain provocations. However, the realization of the full potential of small animal imaging still requires techniques for improving sensitivity, and spatial and temporal resolution. To date, diffuse optical studies of the brain have suffered from several limita-

tions. First, only a limited number of source-detector pairs are often used to collect data. Second, the head is modeled using a simplified model of light propagation in a semi-infinite media. Third, the algorithms for finding the distribution of absorption coefficients in the head assume that the medium in which changes are monitored is homogenous. And, fourth, the reconstructions have only generated 2-D maps, which project superficial and deep effects onto a single plane; hence, no 3-D reconstructions have been performed.

Working toward overcoming these limitations, we present the first 3-D reconstructions of hemodynamics in rats using a model-based iterative image reconstruction (MOBIIR) scheme with data obtained from a dynamic optical tomography (DYNOT) measurement system. We built on our experience with MOBIIR schemes and DYNOT measurement data acquired during our 3-D brain imaging studies in humans. In previous studies we generated 3-D, volumetric reconstructions of the hemodynamic changes that occur during a Valsalva maneuver in the human forehead.<sup>22</sup> For the current studies we have chosen the rat because it is a good model for the elucidation of tissue oxygen saturation, ischemia, and other forms of hemodynamic compromise. In part 1, we investigate global effects of elevated CO<sub>2</sub> levels (hypercapnia) on the cerebral circulation of the rat. In part 2, we focus on localized lateral effects that occur as a result of unilateral carotid occlusion.

This first part is arranged as follows: initially, we introduce the hemodynamic changes that are expected to arise during hypercapnia. This section is followed by a brief description of our instrumentation and probe design. Then, we introduce the image reconstruction algorithm and focus on those aspects that relate to relative measurements, and detail how we incorporated anatomical *a priori* knowledge for enhancing the spatial resolution. Finally, we investigate the system's utility *in vivo* by examining the cerebrovascular hemodynamic response in rats to hypercapnia, and also determine the sensitivity of the reconstruction to inaccurate probe positioning.

## 2 Methods

### 2.1 Instrumentation and Experimental Setup

Measurements on the rat head were performed with a dynamic near-infrared optical tomographic (DYNOT) instrument.<sup>23</sup> This instrument operates in continuous-wave mode. A beam from each of two laser diodes (wavelength = 760 and 830 nm) was sequentially coupled into different multimode fiber bundles (diameter = 1 mm), which deliver the laser light to various positions on the rat head. The laser diodes (high power devices 1110-BUTF-TEC) have a maximum optical output power of 400 mW at the distal end of the fiber but are typically operated at a mean optical output power of 100 mW; the optical power incident on the target is about 30 mW. The lasers are driven by a Newport model 8000 laser controller mainframe housing up to four modules, each serving one laser. Each module provides sinusoidal modulation of the laser diode current with individually selectable frequency and amplitude. The detectors are silicon photodiodes, which provide the required sensitivity, linear response over several orders of magnitude, and ease of operation. Fast detection over a large dynamic range, coupled with fast source switching is achieved by synchronizing adjustment of the detector

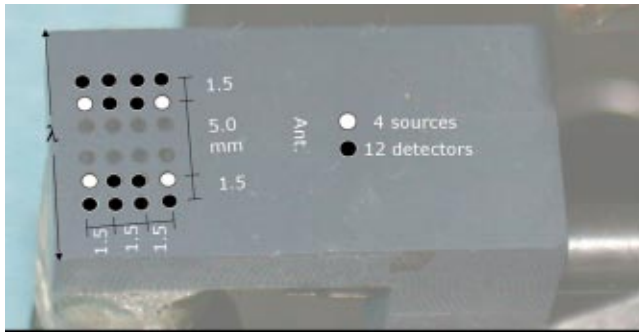


**Fig. 1** Photograph of the surface of our optode probe showing the source (white) and detector (black) locations. The inter-optode spacing was 1.5 mm on-center. 16 fiber optic elements were located in two sets of eight, as shown by the white and black highlights. The left edge of the probe was aligned with the lambda ( $\lambda$ ) suture line.

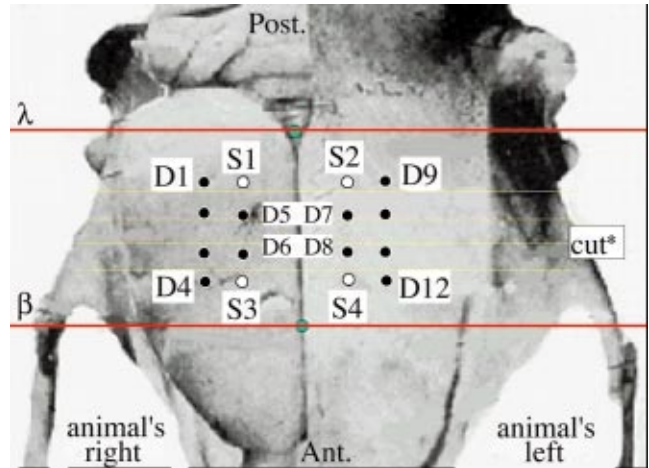


**Fig. 2** The optrode locations relative to the dorsal surface of a rat head. The coronal sections in all figures refer to the slice acquired approximately midway between the bregma and lambda skull sutures (labeled "cut\*").

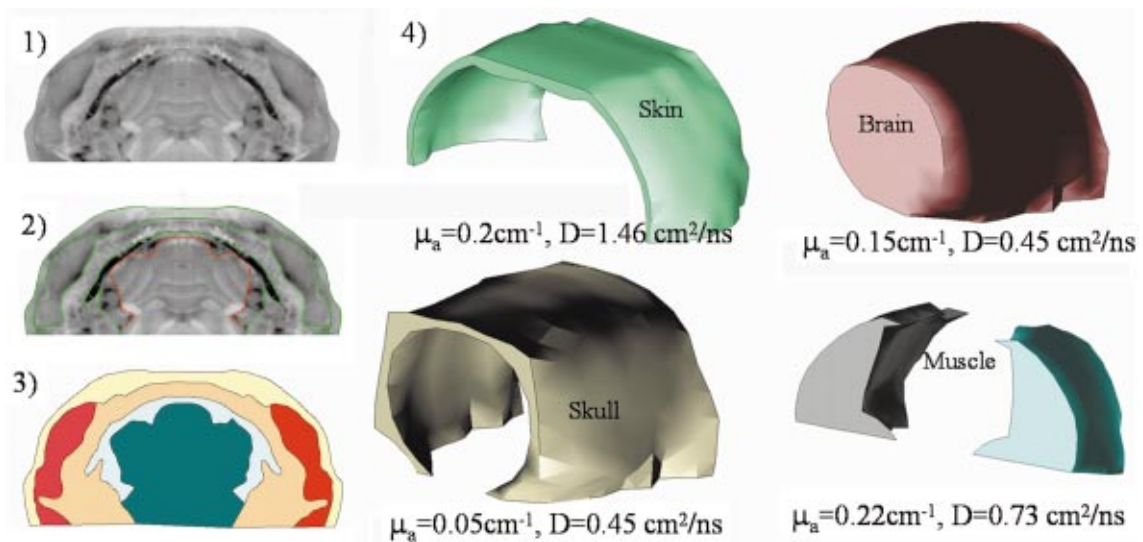


**Fig. 3** Sequence of steps for generating a finite element mesh used in 3-D reconstructions. 1. Cryosection of the top portion of an intact rat head showing the locations of skin, muscle, bone, and brain. 2. Semimanual extraction of boundaries for skin, muscle, bone, and brain regions (green and red outlines). 3. Generation of splines and assignment of tissue-type tags to each layer (skin, muscle, skull, brain). 4. Volumes constructed by connection of multiple coronal sections and the generation of a 3-D layered mesh. The individual layers and the brain were assigned optical coefficients according to the literature (shown next to each layer).

sensitivity for all channels with source movement; thereby providing on-the-fly adaptive gain control. Both source and detector fibers are 1-mm multimode fiber bundles. A more detailed description of the DYNOT instrument can be found in Schmitz et al.<sup>23</sup>

On the target surface, the fibers from the sources and detectors are arranged in a rectangular geometry. The imaging head imbedded with the fibers (Fig. 1) was machined out of a solid piece of opaque (gray-colored) polyethylene. It has an L shape where the base was drilled to accommodate a rod emanating from the stereotaxic  $xyz$  translation unit. The larger surface was drilled with 24 0.8-mm holes in a  $4 \times 6$  uniform grid arrangement. The four source fibers were located at the edges (white circles), and the remainder of the holes were fitted for optical fibers, which were coupled to the detector channels. After cementing all the acrylic fiber optical cables (Fiber Optic Products, Incorporated, Clearlake Oaks, California) in place, the optical surface was smoothed using an optical polishing film, creating a glass-like finish. For the measurements presented in this work, we used four sources and 12 detectors, resulting in  $4 \times 12 = 48$  source-detector combinations. Three full tomographic datasets, involving all 48 source-detector pairs, were acquired per second. A single time point consisted of illuminating each of the four light sources in turn and simultaneously (in parallel) detecting the transmitted light at all of the corresponding 12 detectors. Each time point was acquired in  $\sim 300$  msec, with a single-source and 12-detector acquisition time of 75 msec.

To ensure good contact between the animal's head and the imaging head, we used a modified stereotaxic frame. The head of the rat was secured via two ear bars and an incisor adapter, which secured the upper central incisors to allow for level positioning of the rat head. Our modification to the stereotaxic frame permitted us to position a rat in a supine position with the dorsal surface of the head facing down. The advantage of having a rat in the supine position was that it allowed easier access to the midline neck structures (trachea, carotids) during those experiments described in part 2 of this study. Another key factor in the design of this setup was in imposing a high level of spatial reproducibility in positioning the optical probe on the same anatomical landmark between animals and from day to day. This reproducibility was achieved by placing the entire imaging head on a stereotaxic  $xyz$  translation unit, allowing us to consistently position the edge of the probe in line with the plane formed by the lambda suture line (intra-aural line). Concomitantly, a vertical bar on the imaging head allowed us to position the probe along the midsagittal plane. In experiments where the probe was shifted off midline, the scale on the translation unit was used to measure and adjust the distance from the midline accordingly.

For the sake of clarity, Fig. 2 depicts the position of the probe relative to the dorsal surface of the rat head. All coronal sections presented in the results in Sec. 3 correspond to the slice located approximately midway between the lambda and bregma suture lines and denoted with the word cut\* in the figure.

## 2.2 Image Reconstruction Algorithm

In this work, the 3-D reconstruction of the optical properties in the rat head was achieved using a MOBIIR scheme.<sup>24–27</sup> In

general, a MOBIIR scheme is comprised of three major parts: 1. a forward model that predicts the detector readings based on an assumed spatial distribution of optical properties; 2. an objective function  $\Phi$  that compares predicted with measured signals; and 3. an updating scheme that adjusts the distribution of optical parameters until a certain minimum value of the objective function is achieved.

The forward model, employed in this study is the time-independent diffusion equation, given by:

$$-\nabla D \nabla \phi(r) + c \mu_a \phi(r) = c S(r), \quad (1)$$

where  $\phi$  is the fluence ( $\text{W}/\text{cm}^2$ ), the diffusion coefficient  $D = c/3\mu'_s$  ( $\text{cm}^2/\text{ns}$ ),  $\mu_a$  is the absorption coefficient ( $\text{cm}^{-1}$ ),  $\mu'_s$  is the reduced scattering coefficient ( $\text{cm}^{-1}$ ),  $c$  is the speed of light in tissue ( $22 \text{ cm}/\text{ns}$ ), and  $S$  is the source ( $\text{W}$ ). We incorporated Robin boundary conditions given by

$$c \phi(r) = 2D(r)R \nabla \phi(r), \quad (2)$$

where  $R$  is a factor that takes into account the refractive index mismatch between air and tissue ( $n = 1.4$ ,  $R = 3.24$ ).<sup>28</sup> The partial differential equation (1) was solved using the finite element method.<sup>22</sup>

Our formulation of the MOBIIR scheme requires that predicted detector readings be compared to actual measurements. To this end it is necessary to define an objective function that determines the goodness of fit between measured data  $M$  and predicted detector data  $P$ . Since the DYNOT instrument generates data via a difference-measurement approach, one must compare the change in detector readings between the two states. This approach has two main advantages: first, it is less sensitive to boundary effects, and second, it is less sensitive to the initial guess chosen for the background medium.<sup>29</sup> Intuitively, this can be understood by realizing that in performing a difference measurement, the physical boundary conditions do not change before and after the perturbation. Therefore, in calculating the ratio of light intensity pre- and post-perturbation, the influence of the boundary contribution is minimized. Furthermore, due to the nonlinear relationship between the medium coefficient values and surface detector responses, usually small errors in the selected reference medium can lead to large errors in the computed intensity. However, by projecting the relative change in light intensity to a known reference medium, we normalized out the contribution of the medium and emphasized the contribution of the perturbation, thereby decreasing the sensitivity to the medium's initial distribution. The major disadvantage of this approach is that one cannot determine the absolute distribution of optical properties, only the change in the  $\mu_a$ ,  $\mu'_s$ , or  $D$  from a given baseline. However, many groups have used similar difference-measurement approaches for localizing brain activity and for determining general trends in the oxygenation state.<sup>10,30,31</sup>

To deal with difference data, we have adapted the approach suggested by Pei, Graber, and Barbour,<sup>29</sup> and modified the standard least-square norm objective function to yield:

$$\Phi = \sum_s \sum_d \frac{\left\{ \left[ \frac{M_{s,d}^{\text{pert}(t)}}{M_{s,d}^{\text{ref}}} P_{s,d}(\xi_0) \right] - P_{s,d}(\xi_n) \right\}^2}{\left( \frac{M_{s,d}^{\text{pert}(t)}}{M_{s,d}^{\text{ref}}} P_{s,d}(\xi_0) \right)^2}, \quad (3)$$

where  $s$  and  $d$  refer to sources and detectors, respectively,  $M^{\text{pert}(t)}$  is obtained during the perturbation at a given time  $t$ , and  $M^{\text{ref}}$  is a predetermined reference state. The image reconstruction process is initiated with an initial distribution of optical properties  $\xi_0$ , which is described in further detail in Sec. 2.4 (*a priori* anatomical maps). This initial distribution is updated sequentially, resulting in a new distribution of optical properties  $\xi_n$  at iteration  $n$ . Using this initial distribution of optical properties, the detector readings  $P_{s,d}(\xi_0)$  are calculated with the diffusion forward solver over the domain of interest. These values are then multiplied by the ratio of the perturbation changes  $M_{s,d}^{\text{pert}}/M_{s,d}^{\text{ref}}$  and the value of the objective function  $\Phi$  is determined.

To update the initial distribution of optical properties, we calculate the gradient of the objective function with respect to all optical properties ( $\partial\Phi/\partial\mu_a, \partial\Phi/\partial D$ ). The calculation of the gradient was performed using the technique of adjoint differentiation. This gradient was then used to update the optical properties using an iterative conjugate gradient method. Convergence was usually achieved after 10 to 20 iterations, requiring 2 to 4 hours on a Linux work station with two 500-MHz Pentium III processors. The precise number of iterations for a given reconstruction was dependent on the magnitude of the perturbation (larger in carotid occlusion studies) and the time point selected (larger at times when the magnitude of the change was further from the baseline). Further details on the forward model, objective function, and updating technique using adjoint differentiation can be found in Bluestone et al.<sup>22</sup>

The MOBIIR scheme allowed us to calculate the change in the absorption coefficients produced by a given perturbation. Since all measurements were performed at two wavelengths, each set of reconstructions resulted in a separate change of optical properties  $\Delta\mu_a^{\lambda_1}$  and  $\Delta\mu_a^{\lambda_2}$ . This information was combined by assuming that the primary influence on the changes in the absorption coefficients at each wavelength ( $\lambda$ ) are a linear combination of oxyhemoglobin and deoxyhemoglobin:<sup>32</sup>

$$\Delta\mu_a^\lambda = \varepsilon_{\text{HbO}_2}^\lambda \Delta[\text{HbO}_2] + \varepsilon_{\text{Hb}}^\lambda \Delta[\text{Hb}], \quad (4)$$

where  $\varepsilon_{\text{Hb}}^\lambda, \varepsilon_{\text{HbO}_2}^\lambda$  are the known extinction coefficients for deoxyhemoglobin and oxyhemoglobin at the given wavelengths,<sup>32</sup> respectively. By simultaneously solving the set of algebraic equations at the two wavelengths, we calculated the change in concentration of oxyhemoglobin  $\Delta[\text{HbO}_2]_{\text{meas}}$  and deoxyhemoglobin  $\Delta[\text{Hb}]_{\text{meas}}$  as:

$$\Delta[\text{Hb}]_{\text{meas}} = \frac{\varepsilon_{\text{HbO}_2}^{\lambda_2} \Delta\mu_a^{\lambda_1} - \varepsilon_{\text{HbO}_2}^{\lambda_1} \Delta\mu_a^{\lambda_2}}{\varepsilon_{\text{Hb}}^{\lambda_1} \varepsilon_{\text{HbO}_2}^{\lambda_2} - \varepsilon_{\text{Hb}}^{\lambda_2} \varepsilon_{\text{HbO}_2}^{\lambda_1}}, \quad (5)$$

$$\Delta[\text{HbO}_2]_{\text{meas}} = \frac{\varepsilon_{\text{Hb}}^{\lambda_1} \Delta\mu_a^{\lambda_2} - \varepsilon_{\text{Hb}}^{\lambda_2} \Delta\mu_a^{\lambda_1}}{\varepsilon_{\text{Hb}}^{\lambda_1} \varepsilon_{\text{HbO}_2}^{\lambda_2} - \varepsilon_{\text{Hb}}^{\lambda_2} \varepsilon_{\text{HbO}_2}^{\lambda_1}}. \quad (6)$$

The values of  $\Delta\mu_a^\lambda$  in Eqs. 5 and 6, at each of the two wavelengths, are the calculated changes in the absorption coefficients at each node of the mesh determined using the MOBIIR reconstruction algorithm. Since the reconstruction algorithm determines both  $\Delta\mu_a$  and  $\Delta D$ , it explicitly accounts for the path length between given source-detector positions and reconstructs the predicted values of  $\Delta\mu_a$  and  $\Delta D$  at each node. It should be noted that studies<sup>33–35</sup> have shown that crosstalk between the  $\mu_a$  and  $D \sim 1/\mu_s'$  reconstruction can occur with both continuous-wave and frequency domain instruments. Hence, some of the oxyhemoglobin and deoxyhemoglobin effects may be attributed to scatter changes; therefore, the changes in the hemoglobin parameters are related to the actual values, but the absolute magnitude of the change might not be precisely quantified, since the calculation of a change in one parameter (absorption) could be influenced by a change in another (scatter). In general, researchers assume that during the experiments changes in the scattering coefficient are small compared to changes in the absorption coefficient. This assumption is plausible since we are perturbing blood flow that is more strongly dependent on hemoglobin concentration and oxygenation affecting primarily absorption, rather than perturbing the sampling volume or neuronal tissue, which would primarily influence scatter changes.<sup>36</sup>

### 2.3 *A Priori* Anatomical Maps

NIR diffuse optical tomography suffers from an inherently low spatial resolution. The approach of combining the fine structural information that is available from anatomical maps (e.g., obtained with MRI, CT), with the functional information available from NIR imaging, promises to enhance the spatial resolution.<sup>37,38</sup> To incorporate this concept of anatomical *a priori* information, we used an atlas of a cryo-sectioned rat cranium<sup>39</sup> to obtain an outline of the skin, skull, brain, and muscle tissue. By noting the values for the ear bar locations on the ear bar clamp, during an experiment, we checked head size in each animal and found the interaural distance to be within a millimeter of each other. As a source of variability from animal to animal, such errors will be small compared to other factors such as the details of setting the source/detector probe in exactly the same location with exactly the same “coupling” properties or the general condition of the animal. The segmented 2-D slices of the rat cranium were stitched together to form a 3-D layered volume, which could be used for finite-element-based computation. The total volume of the 3-D mesh was 2761 mm<sup>3</sup>, with the brain volume being 1243 mm<sup>3</sup>. The largest dimension in the horizontal plane was the interaural distance, which was 25 mm, and the maximum vertical distance was 10 mm. After generating the mesh, typical optical properties for 800-nm light were assigned to approximately 2,000 node locations of the tissues, based on the values from the literature.<sup>40</sup> The node locations were assigned absorption coefficients of  $\mu_a = 0.2 \text{ cm}^{-1}$  for skin,  $0.05 \text{ cm}^{-1}$  for skull,  $0.22 \text{ cm}^{-1}$  for muscle, and  $0.15 \text{ cm}^{-1}$  for brain, respectively. The corresponding diffusion coefficients were assigned values of  $D = c/(3\mu_s') = 1.46 \text{ cm}^2/\text{ns}$  for skin,  $0.45 \text{ cm}^2/\text{ns}$  for skull,  $0.73 \text{ cm}^2/\text{ns}$  for muscle, and  $0.45 \text{ cm}^2/\text{ns}$  for brain, respectively (Fig. 3). This information was incorporated into the MOBIIR algorithm, where we modeled NIR tomography measurements consisting of four

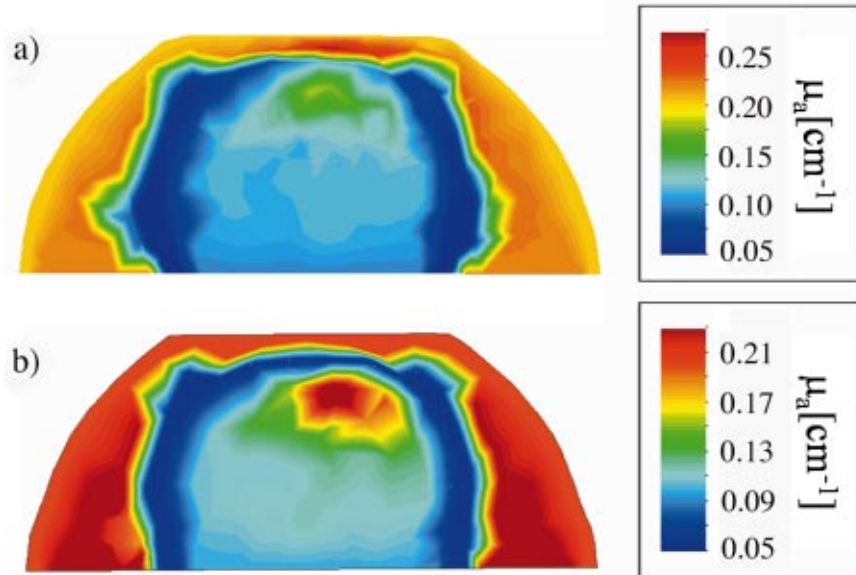


**Fig. 4** Image reconstructions of the location of the simulated optical perturbation shown in Fig. 4 and the benefits of spatial regularization of specific mesh layers. The illustrated coronal sections are taken in the plane of the red line of the upper image in Fig. 4. Part (a) shows the reconstruction of a single perturber in a layered mesh of the rat head without averaging the gradient in the upper three layers. A large increase in signal is seen in the skin layer, and a 30% smaller increase at the correct sight of the perturbation. Part (b) shows the reconstruction result for the case where an average gradient in the top three layers has been imposed. Clearly visible is the improved localization and quality of the image.

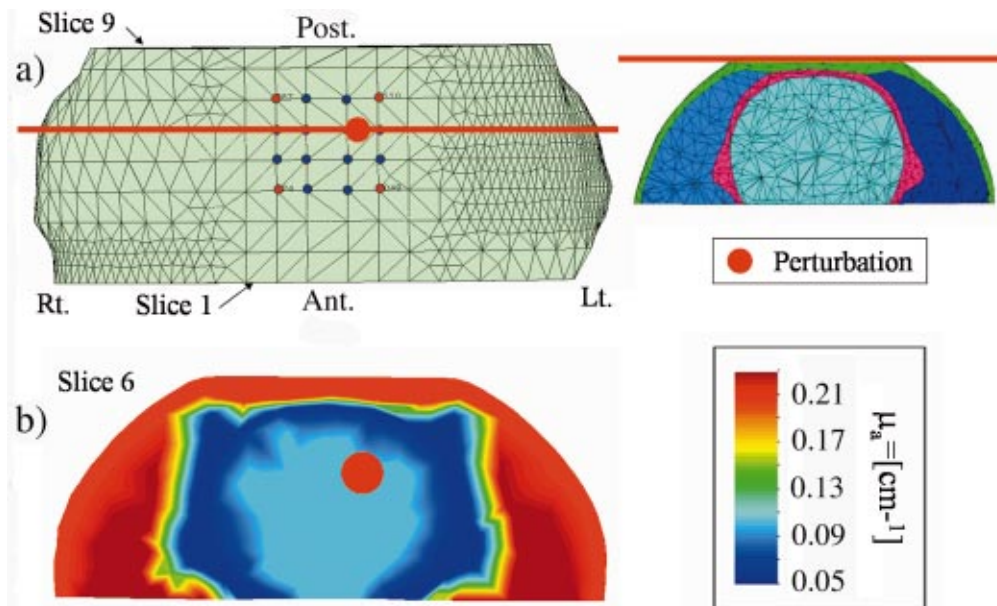


**Fig. 5** Location of a simulated spherical optical perturbation in the right hemisphere of the layered rat head mesh. The upper left figure provides a dorsal view of the mesh, while the upper right figure provides a coronal view of the mesh at the level of the red line. The lower image shows a slice through the head (coronal section) along the red line in the upper left image. The center of the perturber is located 4 mm below the surface. Inside the perturber, the absorption coefficient is 46.7% larger than the background brain parenchyma. Note the gradient is due to interpolation.

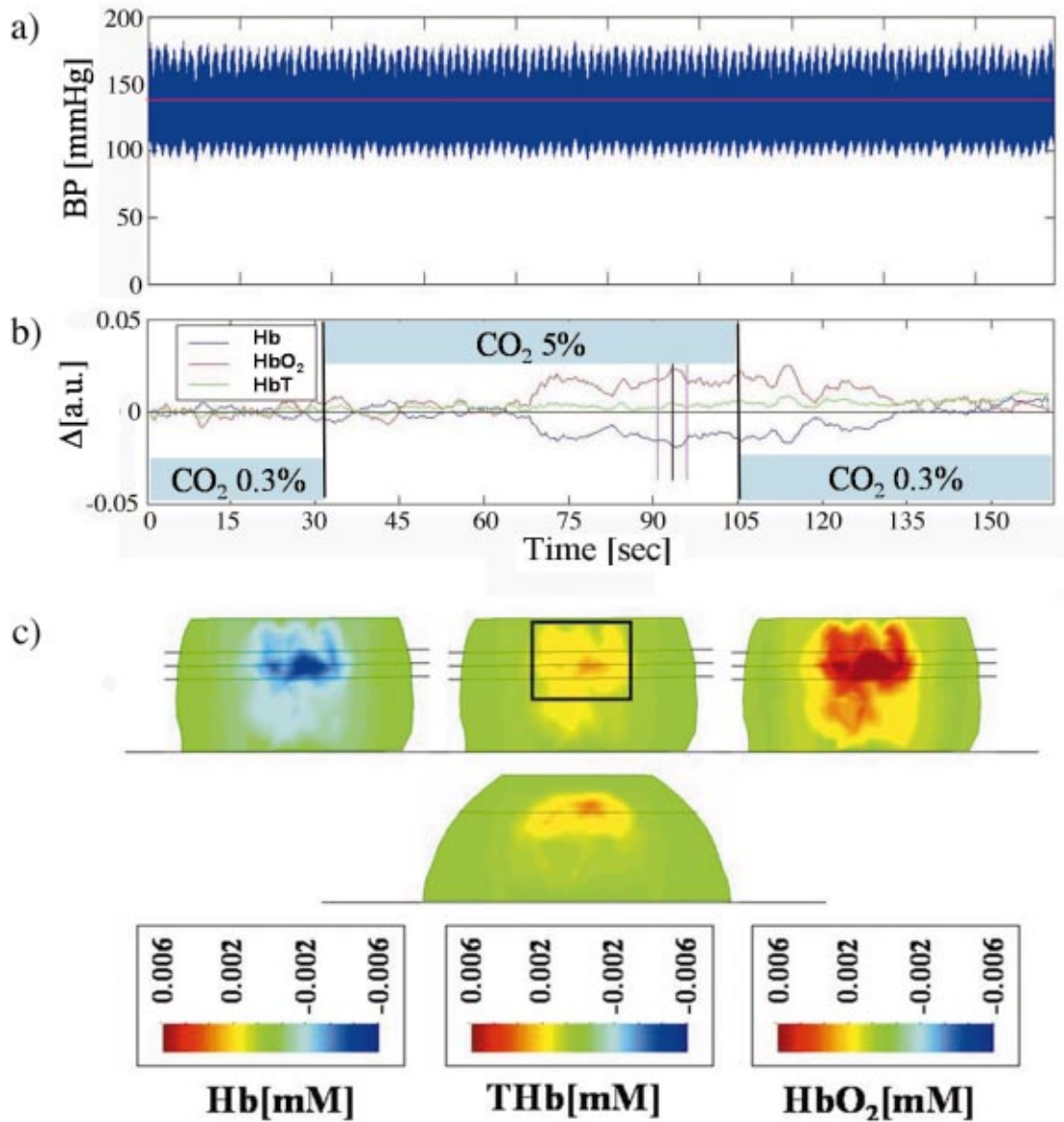


**Fig. 6** Changes in oxyhemoglobin (HbO<sub>2</sub>), deoxyhemoglobin (Hb), and total hemoglobin (THb) in a rat brain during a transient period of hypercapnia. Part (a) shows the stability of the blood pressure. Part (b) displays the change in oxyhemoglobin, deoxyhemoglobin, and blood volume for a single source-detector pair (S1 to D12; see also Fig. 2), as well as the timing of the increase in the inspired CO<sub>2</sub> concentration (light blue blocks, CO<sub>2</sub> increased to 5% between  $t=30$  and 105 sec). In (c), three horizontal sections taken 2 mm below the surface show the change in deoxyhemoglobin, oxyhemoglobin, and total hemoglobin. The coronal section taken at the plane of the middle line in the horizontal sections shows the change in total hemoglobin. These 2-D sections, taken in multiple planes, help visualize the 3-D nature of the reconstruction.

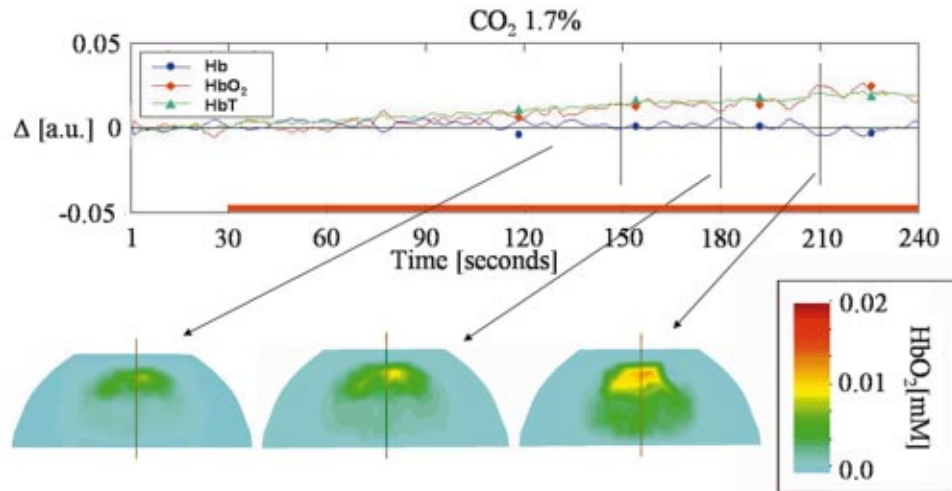


**Fig. 7** Changes in oxyhemoglobin and deoxyhemoglobin in rat brain during a transient period of hypercapnia. Part 1: PaCO<sub>2</sub> changes from 13 to 25 mm Hg. The upper figure shows a signal trace for S1 to D12 during an increase in the inspired CO<sub>2</sub> concentration. The animal was artificially ventilated, such that its baseline CO<sub>2</sub> level was below the normal physiological level (13 mmHg). The CO<sub>2</sub> level was then increased by 1.7%. In the graph one can observe the increase in blood volume and oxyhemoglobin in response to the hypercapnia provocation. The bottom panel shows the global increase in oxyhemoglobin 150, 180, and 210 sec after the initial increase in CO<sub>2</sub>. Blood gas analysis at the plateau (210 to 240) was determined to be 25 mmHg.

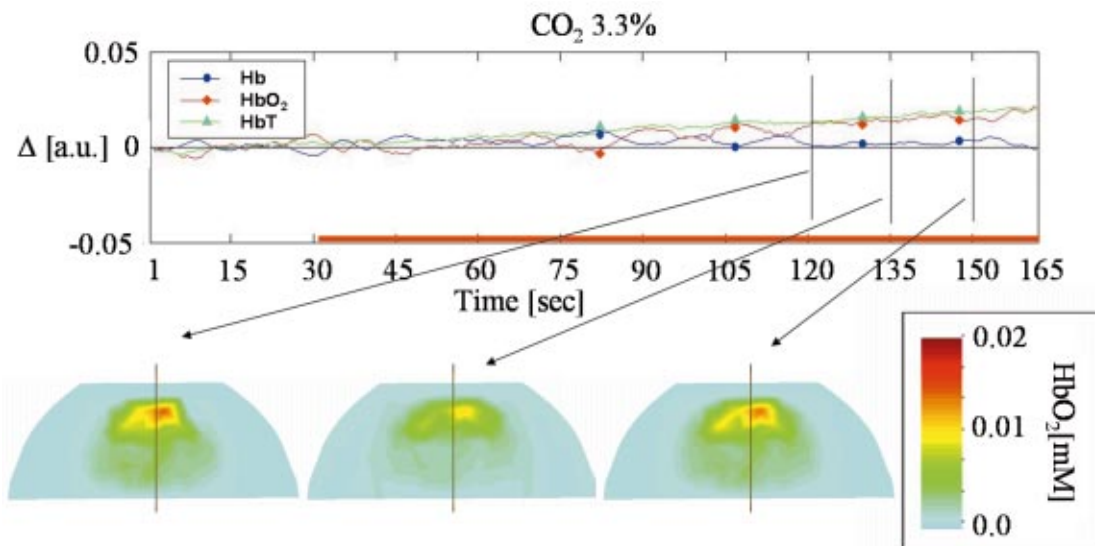


**Fig. 8** Changes in oxyhemoglobin and deoxyhemoglobin in rat brain during a transient period of hypercapnia. Part 2: PaCO<sub>2</sub> changes from 25 to 39 mm Hg. The upper figure shows a signal trace for S1 to D12 during an increase in the inspired CO<sub>2</sub> concentration. The CO<sub>2</sub> level was then increased from 1.7%, shown in Fig. 7, to 3.3%. In the graph, one can observe the increase in blood volume and oxyhemoglobin in response to the hypercapnia provocation. The lower panel shows the global increase in oxyhemoglobin 120, 135, and 150 sec after the initial increase in CO<sub>2</sub>. Blood gas analysis at the plateau (130 to 150) was determined to be 39 mmHg.

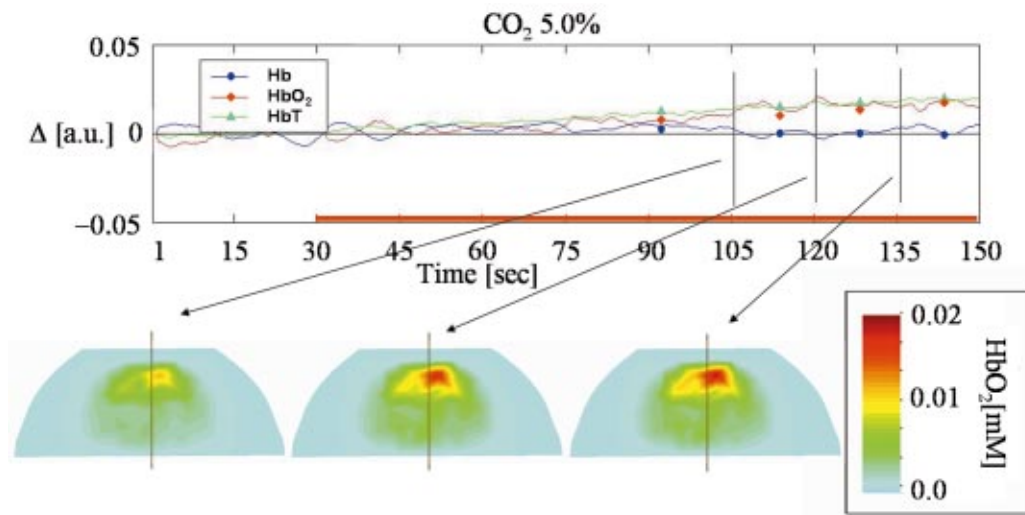


**Fig. 9** Changes in oxyhemoglobin and deoxyhemoglobin in rat brain during a transient period of hypercapnia. Part 3: PaCO<sub>2</sub> changes from 39 to 45 mm Hg. The upper figure shows a signal trace for S1 to D12 during an increase in the inspired CO<sub>2</sub> concentration. The CO<sub>2</sub> level was then increased from 3.3%, shown in Fig. 8, to 5%. In the graph, one can observe the increase in blood volume and oxyhemoglobin in response to the hypercapnia provocation. The lower panel shows the global increase in oxyhemoglobin 105, 120, and 135 sec after the initial increase in CO<sub>2</sub>. Blood gas analysis at the plateau (120 to 150) was determined to be 45 mmHg.

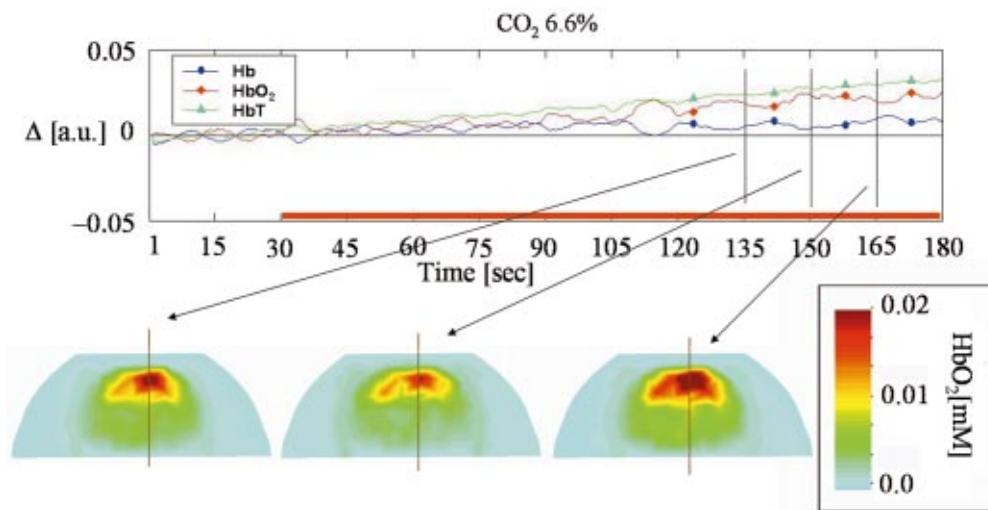


**Fig. 10** Changes in oxyhemoglobin and deoxyhemoglobin in rat brain during a transient period of hypercapnia. Part 4: PaCO<sub>2</sub> changes from 45 to 51 mm Hg. The upper figure shows a signal trace for S1 to D12 during an increase in the inspired CO<sub>2</sub> concentration. The CO<sub>2</sub> level was then increased from 5.0%, shown in Fig. 9, to 6.6%. In the lower graph, one can observe the increase in blood volume and oxyhemoglobin in response to the hypercapnia provocation. The lower panel shows the global increase in oxyhemoglobin 135, 150, and 165 sec after the initial increase in CO<sub>2</sub>. Blood gas analysis at the peak (180 sec) was determined to be 51 mmHg.

sources and 12 detectors located on the rat head, 2-mm rostral to the lambda suture line (see Fig. 2); no noise term was added.

For the experimental studies, the iterative reconstruction was initialized with a layered guess, assuming a homogenous distribution within each layer (coefficients seen in Fig. 3). The reconstruction algorithm was further constrained by averaging the gradient at all nodes within the skin, skull, and muscle layers, respectively. The nodes in the brain volume, however, were allowed to vary independently. In other words, within each of the top three layers, the optical properties changed as a single average unit, between each iteration of the MOBIIR code, while the optical properties at nodes inside the brain changed independent of each other. In this way we avoided reconstruction artifacts close to the optode locations.

To illustrate the advantages of this approach we performed simulations on a model of the rat head depicted in Fig. 4a. We placed an area with an increased absorption coefficient inside the brain, 4 mm below the surface (red dot in Fig. 4b). Using synthetic measurement data, which were generated with and without this area of increased absorption inside the brain, we performed two types of reconstructions. Figure 5a shows the reconstruction without averaging the gradient in the upper three layers between each iteration; while Fig. 5b shows the reconstruction with averaging the gradient in the upper three layers. One can clearly see that the second approach leads to much improved localization of the perturber. This is a reasonable constraint to use in this study, since we are interested in observing spatial variability in the cerebral layer. Furthermore, if a strong vascular response does occur in the upper layers, it will nevertheless be reconstructed, but as a homogeneous increase.

#### 2.4 Animal Preparations and Experimental Protocol

The experiments in this study were designed to look at hemodynamic changes in the head of rats induced by changes in the inspiratory concentration of CO<sub>2</sub>. Under normal conditions, fluctuations in mean arterial (systemic) blood pressure between 60 and 160 mmHg have little effect on cerebral blood flow (CBF), because of the brain's ability to *autoregulate* flow.<sup>41</sup> While systemic blood pressure does not affect CBF, carbon dioxide, pH, and oxygen are potent stimuli to alter cerebral hemodynamics.<sup>42</sup> The relative change in CBF during variations of the partial pressure of carbon dioxide (P<sub>a</sub>CO<sub>2</sub>) depends on several factors, including baseline CBF, cerebral perfusion pressure, and anesthetic drugs.<sup>43</sup> Brain blood flow is not entirely homogeneous, and areas of the brain that receive more blood flow have a steeper flow response to changes in P<sub>a</sub>CO<sub>2</sub>.

In general, the most potent stimulus of brain vasculature is CO<sub>2</sub>. For example, it has been shown that a 7% increase from a physiologic baseline of 0.03% in inhaled CO<sub>2</sub> leads to a doubling of the arteriole diameter.<sup>44</sup> In a wide variety of subjects, most studies report a change in global CBF of 1 to 2 ml/100g/min for each 1 mmHg change in P<sub>a</sub>CO<sub>2</sub>.<sup>45</sup> In awake rats, it has been observed that increasing the P<sub>a</sub>CO<sub>2</sub> to 80 mmHg increases CBF by six times;<sup>46</sup> anesthetics, however, can limit the maximum CBF increase. In urethane-anesthetized rats, a 7.5% increase in inspired CO<sub>2</sub> produced a 30% change in cerebral blood volume (CBV).<sup>47</sup> Some of these

findings have recently been confirmed with functional magnetic resonance imaging<sup>48</sup> as well as with ultrasound Doppler blood velocitometer techniques.<sup>49</sup>

In our studies, five adult male Sprague-Dawley rats, weighing 300 to 325 g, were initially anesthetized with halothane. Then, urethane (1.5 mg/kg; 20% in water; intraperitoneal) was administered as a maintenance anesthetic. A polyethylene catheter was placed in the femoral artery and connected to a blood pressure transducer for continuous monitoring of blood pressure (BP). The output of the BP transducer was amplified and digitized. The intra-arterial line was also used to draw blood for blood gas analysis. The animal was tracheotomized, connected to a mechanical ventilator (Harvard Apparatus, South Natick, Massachusetts), and respirated at a rate of 55 to 65 breaths per minute and a stroke volume of 4 to 5cc.<sup>50</sup> After receiving all the implants, the animal was transferred to the modified stereotaxic frame. The skin overlying the dorsal rat head was shaved and the optical probe was positioned between the anterior and posterior suture lines: bregma and lambda, respectively. Blood pressure was monitored and recorded continuously for the duration of each experiment. When the arterial blood pressure had stabilized, baseline measurements were recorded and then the relative change during a predefined perturbation lasting 1 to 2 min was recorded. This was followed by a recovery period lasting at least 10 min. All experiments and procedures were in accordance with institutional and governmental guidelines.

##### 2.4.1 Ventilation and blood gas analysis

The hypercapnia studies were performed using the inhalation technique. This technique is noninvasive, its response can be well regulated, and it provides a distinct temporal response that is reproducible. The inhalation technique involved varying the inspiratory gas content using computer-controlled precision flow meters (20 ml/min for CO<sub>2</sub>, 1000 ml/min for N<sub>2</sub>, 200 ml/min for O<sub>2</sub>, Dwyer Incorporated). The output from each of the flow meters was fed into a 350 ml mixing chamber before being released to the ventilator input. To test the gas mixer, varying degrees of hypercapnia were induced in the rat. To accomplish this, the CO<sub>2</sub> content was varied, in increments of 1.7%, via a personal computer, between 0 and 6.6%. The O<sub>2</sub> concentration was held fixed at 21%, and the remainder, consisting of nitrogen gas, was adjusted to maintain a fixed total flow rate. At each of the aforementioned CO<sub>2</sub> concentrations, arterial blood was removed from the femoral line and blood gas analysis was performed.

In those experiments where a single concentration of CO<sub>2</sub> was induced, a minimum of 100 images (3/sec) with 0.03% CO<sub>2</sub> (room air) was initially acquired. This was followed by changing the gas concentration for 50 to 100 sec, followed by a return to the baseline gas mixture.

##### 2.4.2 Dose-response studies

In the dose-response experiments, in conjunction with the incremental increases in CO<sub>2</sub>, a blood sample was drawn prior to and immediately after the optical measurements were performed. Specifically, blood was drawn and then a baseline optical measurement was performed. This baseline level was maintained for 30 sec, and then the inspiratory CO<sub>2</sub> concentration was increased by ~1.7% and maintained for the du-

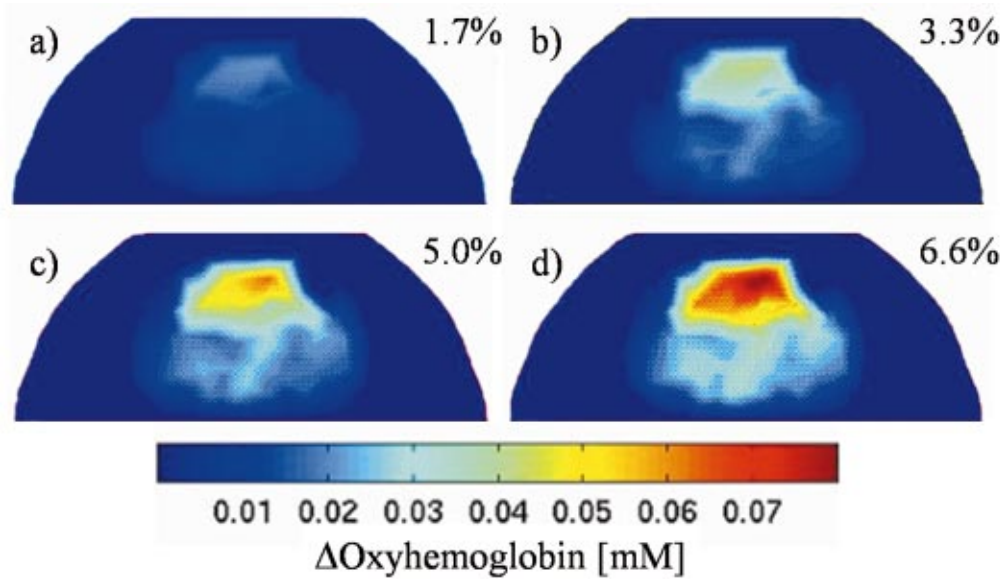


**Fig. 11** Reconstructions of the localized changes in oxyhemoglobin for each of the four changes in CO<sub>2</sub> concentration in a rat that was initially hypocapnic. The relative change in oxyhemoglobin as a function of concentration of CO<sub>2</sub> in an animal that was initially hypocapnic: (a) is at 1.7%, (b) is at 3.3%, (c) is at 5%, and (d) is at 6.6%.

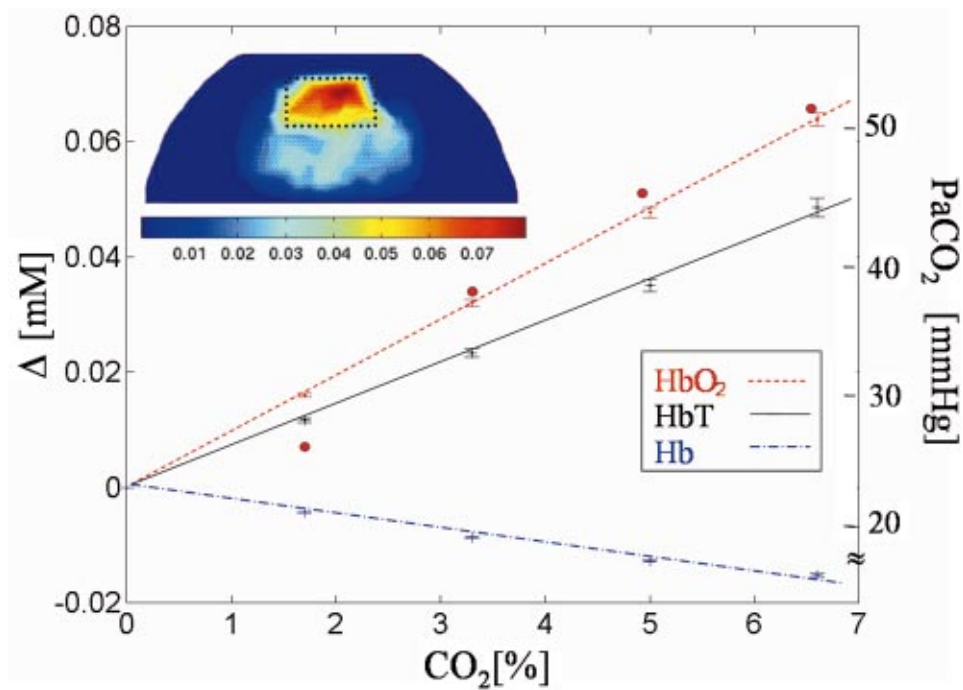


**Fig. 12** Summary of changes in the CO<sub>2</sub> concentration versus changes in deoxyhemoglobin, oxyhemoglobin, and total hemoglobin concentrations starting from an initial hypocapnic state. A region of interest was selected in each of the subfigures in Fig. 11 (inset, rectangular outline), and the mean and standard deviation of the change in each of the hemoglobin parameters was calculated for each image. This was plotted as a function of percent concentration of CO<sub>2</sub>. The red circles display the measured PaCO<sub>2</sub> (right axis) at each of the concentration values of CO<sub>2</sub>.

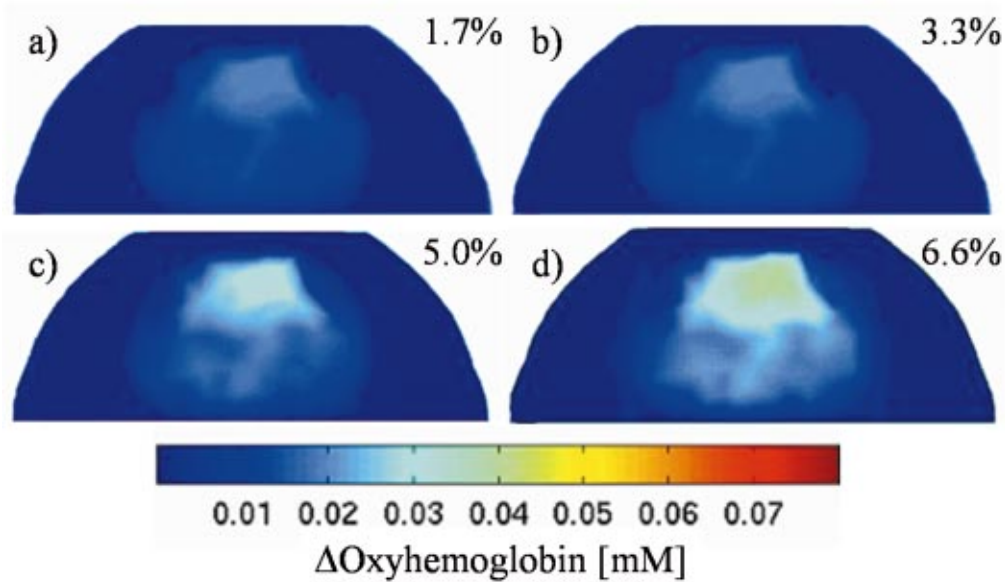


**Fig. 13** Reconstructions of the localized changes in oxyhemoglobin for each of the four changes in CO<sub>2</sub> concentration in a rat that was initially hypercapnic. Upper left image is at 1.7%, upper right at 3.3%, lower left at 5%, and lower right at 6.6%. These images should be compared to those acquired during initial hypocapnia (Fig. 12).

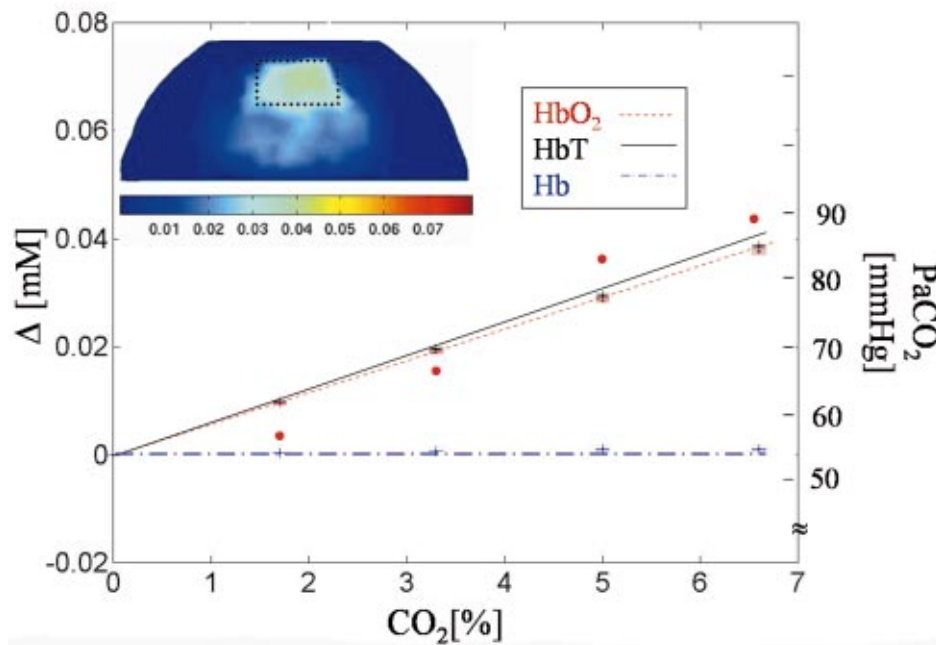


**Fig. 14** Summary of changes in the CO<sub>2</sub> concentration versus changes in deoxyhemoglobin, oxyhemoglobin, and total hemoglobin concentrations starting from an initial hypercapnic state. A region of interest, identical in size and location in each of the subfigures in Fig. 13, was selected (inset, rectangular outline), and the mean and standard deviation of the change in all hemoglobin parameters was calculated for each image. This was plotted as a function of CO<sub>2</sub> and as a function of PaCO<sub>2</sub>.

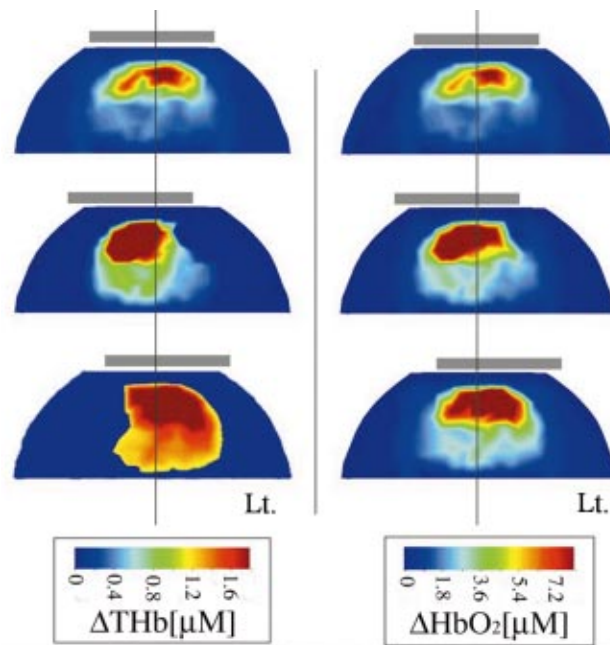


**Fig. 15** Coronal sections for the image reconstructions during hypercapnia under various positional shifts of the probe. The first column shows the increase in total hemoglobin, and the second column shows the increase in oxyhemoglobin. In all reconstructions the model assumes the probe is centered. In the top row, the model matches the experiment (centered), and in the middle row the probe is shifted to the right 1 mm. In the bottom row, the probe is shifted left 1 mm.

ration of the experiment, which lasted  $\sim 240$  sec. We chose a 30-sec baseline period to demonstrate signal stability and a 240-sec observation period, because this was long enough to observe the blood gas changes and the associated respiratory mechanisms for compensation, but short enough to keep renal mechanisms for compensation from complicating the recordings. After termination of the experiment, the arterial femoral catheter was once again used to collect a sample of blood for blood gas analysis. The next experiment began at the previous experiment's final  $\text{CO}_2$  level; hence, each experiment increased the concentration of  $\text{CO}_2 \sim 1.7\%$  above its predecessor.

### 2.4.3 Probe positioning studies

These experiments considered the sensitivity of the reconstruction to inaccuracies in positioning of the probe. Since we had modified a stereotaxic frame to accommodate the optical probe on a  $xyz$  translation unit, we were able to consistently position the edge of the probe in line with the plane formed by the lambda suture line. At the same time, a vertical bar on the imaging head allowed for positioning of the probe along the midsagittal plane. In the probe positioning experiments, the optical probe was shifted to the left and right of midline by 1.0 mm. At each of these new positions, a hypercapnia provocation was induced and measurements were taken. All experiments began at identical physiologic baselines and increased the inspired  $\text{CO}_2$  to 5%.

## 3 Results

### 3.1 Single Concentration Hypercapnia Provocation Study

In Fig. 6, a typical signal change observed during a hypercapnia provocation can be seen. Figure 6(a) shows the stability of the blood pressure during the extent of the experiment. In the blood pressure trace, the peaks are at systolic pressure and the troughs are at diastolic pressure. The mean blood pressure is the average of the systolic and diastolic pressures; note the stability of the mean BP.

In Fig. 6(b) (middle row), the timing of the  $\text{CO}_2$  perturbation is indicated. For the first 30 sec a baseline measurement was recorded. At  $t=30$  sec the concentration of  $\text{CO}_2$  was increased to 5% and maintained at that level for 75 sec. At  $t=105$ , the concentration was returned to the baseline level. The measurements attained at detector 12 with a source at position 1 (source-detector separation of 7 mm) were used to calculate the changes in oxyhemoglobin ( $\text{HbO}_2$ ), deoxyhemoglobin (Hb), and total hemoglobin using the Beer-Lambert law.<sup>51</sup> This calculation was used to generate an easily visualized plot of the change in hemoglobin oxygenation as a function of time. The magnitude of the change was given in arbitrary units (a.u.). Individual trend plots of a single source-detector pair were used to select times of interest, and at those points, full tomographic image reconstructions, using data from all  $4 \times 12 = 48$  source detector pairs, were performed. It is only after performing an image reconstruction that we report concentration changes in the hemoglobin oxygenation as depicted in the coronal sections. One can observe an increase in oxyhemoglobin (red trace), a decrease in deoxyhemoglobin (blue trace), and an increase in total hemoglobin (green trace)

during the  $\text{CO}_2$  provocation. The delayed onset at  $t=65$  sec is caused by a combination of the delay induced by the mixing chamber and the animals' physiologic response. It should be noted that the simultaneous recording of blood pressure (BP) during the experiments eliminated the possibility of the resulting signal change being attributed to perfusion pressure differences.

In Fig. 6(c), horizontal and coronal sections of the change in total, oxyhemoglobin, and deoxyhemoglobin are displayed at time  $t=100$  sec. This figure emphasizes the 3-D nature of the reconstruction. The entire volume beneath the probe was reconstructed using all 48 source-detector combinations. The displayed horizontal sections (top row in Fig. 6c) are 2 mm below the surface of the probe, corresponding to the horizontal line in the coronal section (middle row in Fig. 6c). In these sections one can observe an increase in oxyhemoglobin and total hemoglobin, and a concomitant decrease in deoxyhemoglobin. The single coronal section of the change in total hemoglobin corresponds to the middle black line in the horizontal sections. This is approximately midway between the anterior and posterior extent of the probe (black outlined square in Fig. 6c corresponds to the area underneath the probe). In the remainder of the work, we display coronal sections corresponding to this midway plane. This plane was selected for three main reasons. First, being in the middle, the images are centered in the probing volume and hence can be expected to be most accurate. Second, coronal sections are the ones most often used to visualize lateral affects, as discussed in part 2. Third, by limiting our attention to one plane, it becomes more manageable to observe variation across experiments. All reconstructions in parts 1 and 2 of this work were generated in this fashion; first, full 3-D reconstructions were performed, and then individual planes were selected and visualized.

### 3.2 Dose-Response Studies

In this set of experiments, the percent of inspired carbon dioxide provided to the rat via the artificial respirator was increased by fixed amounts of 1.7, 3.3, 5, and 6.6%. At each of these levels, the partial pressure of  $\text{CO}_2$  in arterial blood was determined using a blood gas analysis machine (ABL 5, Radiometer Medical, Copenhagen, Denmark, 1994). Throughout the experiment, the measured partial pressure of oxygen remained constant at 21%.

In Figs. 7 through 10, the increase in the concentration of  $\text{CO}_2$  occurs after the first 30 sec of the graph and remains elevated for the extent of the experiment (red bar). This step increase leads to a gradual climbing increase in the optical signal, as seen in the figures. In Fig. 7, one can observe the increase in oxyhemoglobin when the  $\text{P}_a\text{CO}_2$  was increased from 13 to 25 mmHg. In Fig. 8, the increase in oxyhemoglobin was induced by increasing the  $\text{P}_a\text{CO}_2$  from a baseline of 25 to 39 mmHg. In Fig. 9, the increase in oxyhemoglobin was induced by increasing the  $\text{P}_a\text{CO}_2$  from a baseline of 39 to 45 mmHg. In Fig. 10, the increase in oxyhemoglobin was induced by increasing the  $\text{P}_a\text{CO}_2$  from a baseline of 45 to 51 mmHg.

As mentioned earlier, we emphasize that the reconstructed images are derived from data on all source-detector pairs, whereas the line graphs show a single source-detector dataset.

The behavior of one source detector pair is useful for showing the time course of changes in relation to experimental manipulations. Such large deviations from baseline appear in all source-detector combinations. “Local” peaks and valleys (such as those marked in Fig. 7) do not appear on all source-detector pairs. Their physiological basis is currently unknown.

The image reconstruction technique that we employ uses relative measurement data. This means that one can only measure changes from a given baseline. In each of the previous four figures from a single rat, the change in CO<sub>2</sub> was relative to the CO<sub>2</sub> concentration at the end of the preceding experiment. To generate a dose-response curve, it was necessary to add the resulting images so that all figures represented a change from a fixed baseline. In Fig. 11, the images have been so generated. Specifically, the upper left image (1.7%) is identical to Fig. 7, the upper right image is the sum of the oxyhemoglobin images in Figs. 7 and 8, the lower left image is the sum of Figs. 7, 8, and 9, etc. Referring to Fig. 11, one can observe an increase in oxyhemoglobin as a function of CO<sub>2</sub> concentration. To quantify this change, a region of interest (ROI) was selected from each image. This ROI was symmetric with respect to the midline and enclosed the upper portion of the brain. Within the ROI, an average change in the oxyhemoglobin concentration was calculated. Similar ROI were selected in the maps of deoxyhemoglobin and total hemoglobin. The resulting graph can be seen in Fig. 12. In the upper left corner of Fig. 12 (inset), the ROI is demarcated by a rectangle. Each point in this graph corresponds to the average value within that rectangular region, and a standard deviation was calculated as well. As one can observe, a linear relationship exists between the inspired CO<sub>2</sub> fraction and average increase in oxyhemoglobin and total hemoglobin, which corresponds to the characteristic increase of the cerebral vascular dilation with increasing depth of hypercapnia.<sup>52</sup>

A second set of experiments was performed, following the same protocol as outlined for the first set, except the animals' baseline level was initially hypercapnic (45 mmHg, instead of 13 mmHg as in the previous case). In Fig. 13, the relative change in oxyhemoglobin as a function of concentration of CO<sub>2</sub> can be seen. Once again, a ROI was selected from each coronal section and a dose-response curve was plotted (Fig. 14). As in Fig. 12, the graph also shows a linear dose response, but the maximum increase in oxyhemoglobin achieved is only half of that in Fig. 12. Also, the relative decrease in deoxyhemoglobin is not as pronounced as that observed in Fig. 12.

### 3.3 Probe Positioning Studies

We also considered the sensitivity of the reconstruction to inaccuracies in proper positioning of the probe. Specifically, we designed a set of experiments to determine the influence of model-experiment mismatch. In other words, if the model assumes the probe is centered, but in the experiment the probe is slightly off-center, how will the reconstruction appear? To model this mismatch, we accurately positioned the probe on the same anatomical landmark.

In Fig. 15, three sets of data are shown. In the top row, the probe was centered (gray bar) and the model assumed the probe was centered. As one can see, the increase in total hemoglobin and oxyhemoglobin is approximately symmetric

with respect to the midsagittal plane. In the second row, the probe was shifted to the right but the model assumed the probe was centered. As one can see, the increase in total hemoglobin and oxyhemoglobin is now pulled to the side of the probe. In the third row, the probe was shifted to the left and the model assumed the probe was centered. In this case one can see that the reconstructions are pulled to the left. As a result of these experiments, one can observe that shifts of the probe position, as small as 1 mm influence the spatial localization in the reconstruction.

## 4 Discussion

In this first part of the study, we show that utilizing a DYNOT imager adapted for small animal imaging, together with a 3-D MOBIIR algorithm, allows for the volumetric visualization of global changes in the vascular hemodynamics in the rat brain during hypercapnia. These changes were induced by varying the inspiratory gas mixture. In all the experiments, an optical signal was observed and images at select time points were generated.

Using a computer-controlled multigas flow meter, we experimentally observed an increase in the oxyhemoglobin concentration when arterial blood P<sub>a</sub>CO<sub>2</sub> was raised from 13 to 51 mmHg in increments of 10 to 15 mmHg. We found that an approximately linear relationship exists within any given rat. The particular rate of increase, however, depends on the starting condition (physiological baseline) of the experiment. This finding was made explicit by starting from a blood pressure of 13 mmHg in one experimental set of measurements, and from 45 mmHg in a second experimental set (compare maximum oxyhemoglobin increase in Fig. 12 with Fig. 14). While quantitative measurements are baseline dependent, the spatial distribution is comparable. Specifically, the increase in total hemoglobin appears on average to equally affect both cerebral hemispheres below the probe, irrespective of the starting P<sub>a</sub>CO<sub>2</sub>. It was expected that maximum dilation would lead to a larger relative change in total hemoglobin in the rat that was initially hypocapnic, and this was indeed observed (Fig. 12). All these observations agree with known physiological responses to hypercapnia.<sup>52</sup> Furthermore, despite the fact that the image reconstruction technique that we employ uses relative measurement data (i.e., one can only measure changes from a given baseline), as shown in Figs. 12 and 14, one can still make quantitative statements (linear dose response) with regard to these changes within a given animal and predefined starting condition. Hence, by generating a dose-response curve to varying degrees of hypercapnia, we have shown that this type of measurement data contains useful information and can be used to gauge the progression of change in cerebral hemodynamics.

The inherently low spatial resolution of optical tomography was enhanced by using the structural information of an atlas to build a layered mesh of the rat head. Different tissues were assigned optical properties based on literature values. This model was used as a starting point for all image reconstructions. Furthermore, the surface artifacts known to arise when using back-reflected light was reduced by applying an average layered gradient to the uppermost layers, while allowing the nodes within the brain to vary independently. This

technique was tested on simulated data and applied to the experimental results as well.

The probe positioning studies considered the sensitivity of the reconstruction to inaccuracies in proper optical probe positioning. We found that inaccuracies as small as 1 mm or 1/10 of the maximum source-detector separation tend to shift the image toward the probe, creating what appears to be a lateralized affect. This experiment-model mismatch must be carefully excluded when trying to observe phenomenon that one expects to be lateralized.

## 5 Summary

Using model-based iterative image reconstruction schemes (MOBIIR) in combination with data obtained from a dynamic optical tomographic imaging instrument, we are able to visualize global vascular dynamics in the rat brain during controlled changes in the amounts of inspired carbon dioxide. The changes in oxyhemoglobin, deoxyhemoglobin, and blood volume are linearly related to the fraction of CO<sub>2</sub>. As expected, the increase in cerebral total hemoglobin is found to be present over the entire cortex, and appears to be symmetric with respect to the midsagittal plane. The results obtained here for a model of cerebral vasoreactivity to hypercapnia in a rat are in reasonable agreement with the data from the literature,<sup>53</sup> and offer the potential for further validation with more focal phenomenon, which will be the focus of part 2 of this study.

## Acknowledgments

This work was supported in part by the National Heart, Lung, and Blood Institute (NHLBI-grant number 2R44-HL-61057-02A1, Andreas Hielscher), and the National Institute of Neurological Disorders and Stroke (NINDS-grant number NS045160, NS382090, Mark Stewart) both part of the National Institutes of Health (NIH), the City of New York Council Speaker's Fund for Biomedical Research: Toward the Science of Patient Care, and the Dean's Office of the College of Medicine at the State University of New York (SUNY) Downstate Medical Center in Brooklyn, New York.

## References

1. T. F. Budinger, D. A. Benaron, and A. P. Koretsky, "Imaging transgenic animals," *Ann. Biomed. Eng.* **1**, 611–648 (1999).
2. R. Weissleder and U. Mahmmod, "Molecular imaging," *Radiology* **219**, 316–333 (2001).
3. M. J. Paulus, S. S. Gleason, and M. Easterly, "A review of high-resolution x-ray computed tomography and other imaging modalities for small animal research," *Lab Anim.* **30**, 36–45 (2001).
4. R. Weissleder, C. H. Tung, U. Mahmood, and A. Bogdanov, Jr., "In vivo imaging of tumors with protease-activated near-infrared fluorescent probes," *Nat. Biotechnol.* **17**, 375–378 (1999).
5. U. Mahmood, C. H. Tung, A. Bogdanov, Jr., and R. Weissleder, "Near-infrared optical imaging of protease activity for tumor detection," *Radiology* **213**, 866–870 (1999).
6. T. J. Sweeney, V. Mailander, A. A. Tucker, A. B. Olomu, W. S. Zhang, Y. A. Cao, R. S. Negrin, and C. H. Contag, "Visualizing the kinetics of tumor-cell clearance in living animals," *Proc. Natl. Acad. Sci. U.S.A.* **96**, 12044–12049 (1999).
7. C. H. Contag, D. Jenkins, P. R. Contag, and R. S. Negrin, "Use of reporter genes for optical measurements of neoplastic disease in vivo," *Neoplasia* **2**, 41–52 (2000).
8. C. H. Contag, S. D. Spilman, P. R. Contag, M. Oshiro, B. Eames, P. Dennery, D. K. Stevenson, and D. A. Benaron, "Visualizing gene expression in living mammals using a bioluminescent reporter," *Photochem. Photobiol.* **66**, 523–531 (1997).
9. V. Ntziachristos and R. Weissleder, "Experimental three-dimensional fluorescence reconstruction of diffuse media by use of a normalized Born approximation," *Opt. Lett.* **26**, 893–895 (2001).
10. D. A. Benaron, S. R. Hintz, A. Villringer, D. Boas, A. Kleinschmidt, J. Frahm, C. Hirth, H. Obrig, J. C. Van Houten, E. L. Kermit, W. Cheong, and D. K. Stevenson, "Noninvasive functional imaging of human brain using light," *J. Cereb. Blood Flow Metab.* **20**, 469–477 (2000).
11. E. Watanabe, A. Maki, F. Kawaguchi, Y. Yamashita, H. Koizumi, and Y. Mayanagi, "Noninvasive cerebral blood volume measurement during seizures using multichannel near infrared spectroscopic topography," *J. Biomed. Opt.* **5**, 287–290 (2000).
12. M. Franceschini, V. Toronov, M. E. Filiaci, E. Gratton, and S. Fantini, "On-line optical imaging of the human brain with 160-ms temporal resolution," *Opt. Express* **6**, 49–57 (2000).
13. A. Kleinschmidt, H. Obrig, M. Requardt, K. Merboldt, U. Dirnagl, A. Villringer, and J. Frahm, "Simultaneous recording of cerebral blood oxygenation changes during human brain activation by magnetic resonance imaging and near infrared spectroscopy," *J. Cereb. Blood Flow Metab.* **16**, 817–826 (1996).
14. S. R. Hintz, W. F. Cheong, J. P. van Houten, D. K. Stevenson, and D. A. Benaron, "Bedside imaging of intracranial hemorrhage in the neonate using light: comparison with ultrasound, computed tomography, and magnetic resonance imaging," *Pediatr. Res.* **45**, 54–59 (1999).
15. T. Wolf, U. Lindauer, H. Obrig, J. Dreier, T. Back, A. Villringer, and U. Dirnagl, "Systemic nitric oxide synthase inhibition does not affect brain oxygenation during cortical spreading depression in rats: A non-invasive near-infrared spectroscopy and laser-doppler flowmetry study," *J. Cereb. Blood Flow Metab.* **16**, 1100–1107 (1996).
16. T. Wolf, U. Lindauer, U. Reuter, T. Back, A. Villringer, K. Einhäupl, and U. Dirnagl, "Noninvasive near infrared spectroscopy monitoring of regional cerebral blood oxygenation changes during peri-infarct depolarization in focal cerebral ischemia in the rat," *J. Cereb. Blood Flow Metab.* **17**, 950–954 (1997).
17. M. Nemoto, Y. Nomura, C. Sato, M. Tamura, K. Houkin, I. Koyanagi, and H. Abe, "Analysis of optical signals evoked by peripheral nerve stimulation in rat somatosensory cortex: dynamic changes in hemoglobin concentration and oxygenation," *J. Cereb. Blood Flow Metab.* **19**, 246–259 (1999).
18. A. M. Siegel, J. J. A. Marota, and D. A. Boas, "Design and evaluation of a continuous-wave diffuse optical tomography system," *Opt. Express* **4**, 287–298 (1999).
19. C. Cheung, J. P. Culver, K. Takahashi, J. H. Greenberg, and A. G. Yodh, "In vivo cerebrovascular measurement combining diffuse near-infrared absorption and correlation spectroscopies," *Phys. Med. Biol.* **46**, 2053–2065 (2001).
20. C. Wei-Guo, L. I. Peng-Cheng, L. Qing-Ming, Z. Shao-Qun, and H. Bo, "Hemodynamic assessment of ischemic stroke with near-infrared spectroscopy," *Space Med. Medical Eng.* **13**, 84–89 (2000).
21. C. Weiguo, L. Guang, and W. Lichty, "Localizing the focus of ischemic stroke with near infrared spectroscopy," *Chin. Med. J. (Engl)* **115**, 84–88 (2002).
22. A. Y. Bluestone, G. Abdoulaev, C. H. Schmitz, R. L. Barbour, and A. H. Hielscher, "Three-dimensional optical tomography of hemodynamics in the human head," *Opt. Express* **9**, 272–286 (2001).
23. C. H. Schmitz, M. Locker, J. M. Lasker, A. H. Hielscher, and R. L. Barbour, "Instrumentation for fast functional optical tomography," *Rev. Sci. Instrum.* **73**, 1–11 (2002).
24. A. H. Hielscher, A. D. Klose, and K. M. Hanson, "Gradient-based iterative image reconstruction scheme for time-resolved optical tomography," *IEEE Trans. Med. Imaging* **18**, 262–271 (1999).
25. A. D. Klose and A. H. Hielscher, "Iterative reconstruction scheme for optical tomography based on the equation of radiative transfer," *Med. Phys.* **26**, 1698–1707 (1999).
26. R. Roy and E. M. Sevick-Muraca, "Truncated Newton's optimization scheme for absorption and fluorescence optical tomography: Part I Theory and formulation," *Opt. Express* **4**, 353–371 (1999).
27. S. R. Arridge and M. Schweiger, "A gradient-based optimization scheme for optical tomography," *Opt. Express* **2**, 213–226 (1998).
28. A. H. Hielscher, S. L. Jacques, L. Wang, and F. K. Tittel, "The influence of boundary conditions on the accuracy of diffusion theory in time-resolved reflectance spectroscopy of biological tissues," *Phys. Med. Biol.* **40**, 1957–1975 (1995).
29. Y. Pei, H. L. Graber, and R. L. Barbour, "Influence of systematic

- errors in reference states on image quality and on stability of derived information for DC optical imaging," *Appl. Opt.* **40**, 5755–5769 (2001).
30. A. Villringer and B. Chance, "Non-invasive optical spectroscopy and imaging of human brain function," *Trends Neurosci.* **20**, 435–442 (1997).
  31. D. A. Boas, T. Gaudette, G. Strangman, X. Cheng, J. J. Marota, and J. B. Mandeville, "The accuracy of near infrared spectroscopy and imaging during focal changes in cerebral hemodynamics," *Neuroimage* **13**, 76–90 (2001).
  32. S. Wray, M. Cope, and D. T. Delpy, "Characteristics of the near infrared absorption spectra of cytochrome  $aa_3$  and hemoglobin for the noninvasive monitoring of cerebral oxygenation," *Biochim. Biophys. Acta* **933**, 184–192 (1988).
  33. S. R. Arridge and M. Schweiger, "A gradient-based optimization scheme for optical tomography," *Opt. Express* **2**, 213–226 (1998).
  34. T. O. McBride, B. W. Pogue, U. L. Osterberg, and K. D. Paulsen, "Separation of absorption and scattering heterogeneities in NIR tomographic imaging of tissues," *OSA Tech. Digest*, pp. 339–341 (2000).
  35. Y. Pei, H. L. Graber, and R. L. Barbour, "Normalized-constraint algorithm for minimizing inter-parameter crosstalk in DC optical tomography," *Opt. Express* **9**, 97–109 (2001).
  36. H. Obrig and A. Villringer, "Beyond the visible—Imaging the human brain with light," *J. Cereb. Blood Flow Metab.* **23**, 1–18 (2003).
  37. B. Pogue and K. Paulsen, "High-resolution near-infrared tomographic imaging simulations of the rat cranium by use of a priori magnetic resonance imaging structural information," *Opt. Lett.* **23**, 1716–1718 (1998).
  38. A. H. Hielscher and S. Bartel, "Use of penalty terms in gradient-based iterative reconstruction schemes for optical tomography," *J. Biomed. Opt.* **6**, 183–192 (2001).
  39. A. W. Toga, E. M. Santori, R. Hazani, and K. Ambach, "A 3D digital map of rat brain," *Brain Res. Bull.* **38**, 77–85 (1995).
  40. A. H. Hielscher, R. E. Alcouffe, and R. L. Barbour, "Comparison of finite-difference transport and diffusion calculations for photon migration in homogeneous and heterogeneous tissues," *Phys. Med. Biol.* **43**, 1285–1302 (1998).
  41. S. Newman, S. Gilman, J. Manter, and A. Gatz, *Manter and Gatz's Essentials of Clinical Neuroanatomy and Neurophysiology*, R. G. Clark, Ed., F. A. Davis Co., Philadelphia (2002).
  42. M. Reivich, "Arterial  $PCO_2$  and cerebral hemodynamics," *Am. J. Physiol.* **206**, 5–35 (1964).
  43. C. Iadecola and F. Zhang, "Nitric oxide-dependent and -independent components of cerebrovasodilation elicited by hypercapnia," *Am. J. Physiol.* **266**, R546–R552 (1994).
  44. L. Edvinsson, "The physiological basis," in *Cerebral Blood Flow and Metabolism*, pp. 161–162, Raven Press, New York (1993).
  45. M. Reivich, "Arterial  $PCO_2$  and cerebral hemodynamics," *Am. J. Physiol.* **206**, 25–35 (1964).
  46. L. Berntman, N. Dahlgren, and B. K. Siesjo, "Cerebral blood flow and oxygen consumption in the rat brain during extreme hypercapnia," *Anesthesiology* **50**, 299–305 (1979).
  47. G. H. Wu, F. Luo, and Z. Li, "Transient relationships among BOLD, CBV, and CBF changes in rat brain as detected by functional MRI," *Magn. Reson. Med.* **48**, 987–993 (2002).
  48. P. Van Zijl, S. Eleff, J. A. Vlatowski, J. M. E. Oja, A. M. Ulug, R. J. Troystman, and R. A. Kavppinen, "Quantitative assessment of blood flow, blood volume and blood oxygenation effects in functional magnetic resonance imaging," *Nat. Med.* **4**, 159–167 (1998).
  49. A. Hauge, M. Thoresen, and L. Walloe, "Changes in cerebral blood flow during hyperventilation and  $CO_2$ -breathing measured transcutaneously in humans by a bi-directional, pulsed, ultrasound Doppler blood velocimeter," *Acta Physiology Scand.* **111**, 167–173 (1980).
  50. *Experiments and Surgical Technique in the Rat*, H. B. Waynforth and P. A. Flecknell, Eds., Academic Press, San Diego, CA (1992).
  51. B. L. Horecker, "The absorption spectra of hemoglobin and its derivatives in the visible and near-infrared regions," *J. Biol. Chem.* **148**, 173–184 (1943).
  52. R. L. Grubb, M. E. Raichle, J. O. Eichling, and M. M. Ter-Pogossian, "The effects of changes in  $P_aCO_2$  on cerebral blood volume, blood flow, and vascular mean transit time," *Stroke* **5**, 630–639 (1974).
  53. R. Totaro, G. Barattelli, V. Quaresima, A. Carolei, and M. Ferrari, "Evaluation of potential factors affecting the measurement of cerebrovascular reactivity by near-infrared spectroscopy," *Clin. Sci.* **95**, 497–504 (1998).